# On the role of Fe(III) ions on the Reduction Mechanisms of Concentrated Nitric Acid

J. Pellé, N. Gruet, B. Gwinner, M. Schlegel, Vincent Vivier

# On the role of Fe(III) ions on the Reduction Mechanisms of Concentrated Nitric Acid

J. Pellé[1,2], N. Gruet[2], B. Gwinner[2], M. Schlegel[3], V. Vivier[1]

[1]Sorbonne Université, CNRS, Laboratoire Interfaces et Systèmes Electrochimiques, 4 place Jussieu, F-75005, Paris, France

[2]Den – Service de la Corrosion et du Comportement des Matériaux dans leur Environnement (SCCME), CEA, Université Paris-Saclay, F-91191, Gif-sur-Yvette, France

[3]Den – Service d'Etudes Analytiques et de Réactivité des Surfaces (SEARS), CEA, Université Paris-Saclay, F-91191, Gif-sur-Yvette, France

**Abstract**

The reduction mechanism of concentrated $HNO_3$ (4 mol $L^{-1}$) was investigated on a gold electrode at 40 °C by coupling electrochemical methods (cyclic voltammetry, chrononamperometry and electrochemical impedance spectroscopy) with chemical analysis of solution by Raman spectroscopy and the gas analysis by mass spectrometry. It was demonstrated that in such conditions, Fe(III) promotes the catalytic reduction reactions of concentrated $HNO_3$. This was ascribed to the fact that Fe(III) modifies the chemical equilibrium in concentrated nitric acid by generating reduced species of nitric acid such as $NO_2$. Then, the presence of these species catalyses the reduction of nitric acid with a mechanism which can tuned depending on the concentration in Fe(III) and the applied potential.

**Keywords:** Electrochemical impedance spectroscopy; Autocatalytic mechanism; Nitrate reduction reaction; Iron ion catalysis

## 1. Introduction

In the French spent-nuclear-fuel reprocessing plants, the PUREX process (Plutonium and Uranium Refining EXtraction) is commonly used, in which the fuel is dissolved in nitric acid [1, 2]. In the different steps of this process, nitric acid is used at various concentrations, up to the azeotrope level (14.4 mol $L^{-1}$) and at different temperatures, up to the boiling temperature (*i.e.* 120 °C). In addition to these very acidic properties, nitric acid also acts as a strong oxidizing agent, which requires a careful selection of installation materials such as stainless steel (SS) grade which is a material commonly used in the nuclear industry for its resistance to these severe corrosive conditions. However, in the case of stagnant nitric acid the corrosion increases and intergranular corrosion can develop [3-5]. It has been shown in a previous work [6] that an increase of the corrosion rate of SS without renewal of the electrolyte can be ascribed to the accumulation of dissolution products in solution (*e.g.* Fe(III), Cr(III), Ni(II)). It was shown that the presence of Fe(III) in nitric solution leads to an increase of the cathodic current and to a shift of the corrosion potential toward the transpassive domain, where intergranular corrosion occurs.

Therefore, in order to gain a better understanding of the role of Fe(III) on the cathodic reactions, it is necessary to first understand the reduction mechanisms of nitric acid free of contaminating ions. An elegant approach has been developed independently by Vetter and Schmid in the 50's by studying the reduction mechanism on platinum for nitric acid concentrations in the range of 1 to 10 mol $L^{-1}$ [7-15]. For concentrated solutions, it has been shown that many species, including $NO_2$ and $NO^+$, exist as soluble and gas species involving different chemical equilibriums [16].

According to Vetter [7-9], the reduction of concentrated $HNO_3$ follows a heterogeneous mechanism. The regeneration of $NO_2$ species (valence IV for nitrogen), which is assumed to be the electroactive species (3), occurs at the electrode with a slow heterogeneous kinetics (5). In

such a case, the current density as a function of the rotation rate of the rotating disk-electrode (RDE) used for performing the study follows the classical Levich's equation, and the analysis of the results have led to the following mechanism:

$$NO^{+}_{(ads)} + NO_3{}^{-}_{(ads)} \leftrightarrow N_2O_{4\,(ads)} \quad (1)$$

$$N_2O_{4(ads)} \leftrightarrow 2NO_{2\,(ads)} \quad (2)$$

$$NO_{2\,(ads)} + e^{-} \leftrightarrow NO_2{}^{-}_{(ads)} \quad (3)$$

$$NO_2{}^{-}_{(ads)} + H^{+} \leftrightarrow HNO_{2\,(ads)} \quad (4)$$

$$HNO_{2\,(ads)} + H^{+} \leftrightarrow NO^{+}_{(ads)} + H_2O_{(l)} \quad (5)$$

Conversely, Schmid proposed a homogeneous reduction mechanism for concentrated $HNO_3$. In this case, $NO^+$ (valence III for nitrogen) is believed to be the electroactive species (8). The $NO^+$ species form an acid-base equilibrium with $HNO_2$ in solution (6). The reduction of $NO^+$ produces NO that can be oxidized back by $HNO_3$ in solution to form $HNO_2$ (10). An autocatalytic process can take place depending on the hydrodynamic conditions at the electrode since these species must remain in the close vicinity of the electrode surface to further react. As a results, an unexpected current density variation as a function of the rotation rate of RDE is observed: the higher the rotation rate of the RDE, the lower the current density [17]. Similarly, Lange has shown that the size of the electrode has also a significant impact on the Schmid's mechanism [18]. This can be explained by the fact that for macroscopic electrodes, linear diffusion takes places and mass transfer is less efficient than on microelectrodes (hemispheric diffusion) [19], on which the autocatalytic mechanism of concentrated nitric acid can no longer be observed. The following mechanism was thus proposed:

$$2HNO_{2(aq)} + 2H^{+}{}_{(aq)} \leftrightarrow 2NO^{+}{}_{(aq)} + 2H_2O_{(l)} \quad (6)$$

$$2NO^{+}{}_{(aq)} \leftrightarrow 2NO^{+}{}_{(ads)} \quad (7)$$

$$2NO^{+}{}_{(ads)} + 2e^{-} \leftrightarrow 2NO_{(ads)} \quad (8)$$

$$2NO_{(ads)} \leftrightarrow 2NO_{(aq)} \quad (9)$$

$$2NO_{(aq)} + HNO_{3(aq)} + H_2O \leftrightarrow 3HNO_{2(aq)} \quad (10)$$

Later, Razygraev *et al.* [15] investigated this mechanism in boiling nitric acid solutions (2 mol $L^{-1}$) at a platinum electrode. They showed that both mechanisms can occur, depending on the cathodic overpotential applied to the inert electrode. For the lower cathodic overpotentials (0.85 V/SHE < $E$ < 1.15 V/SHE), the Vetter's mechanism prevails, whereas for the higher overpotentials (0.65 V/SHE < $E$ < 0.85 V/SHE) the Schmid's mechanism is observed. For the potentials smaller than 0.65 V/SHE, a significant decrease 'in absolute value) in current density was observed, which was ascribed to the reduction of NO to $N_2O$ following reaction (11) thereby stopping the autocatalytic Schmid's mechanism.

$$2NO_{(ads)} + 2H^{+}{}_{(aq)} + 2e^{-} \leftrightarrow N_2O_{(ads)} + H_2O \quad (11)$$

Balbaud *et al.* [20] also studied the influence of the concentration of nitric acid on the reduction mechanism using a platinum electrode at 100 °C. Similarly to the Schmid's mechanism, they devised a mechanism with $HNO_2$ as electroactive specie (12), which is formed back in solution following a chemical step involving $HNO_3$ (13) or (14). Two different reaction mechanisms were proposed depending on the concentration of nitric acid. For [$HNO_3$] < 8 mol $L^{-1}$:

$$HNO_{2\,(ads)} + H^{+}_{(aq)} + e^{-} \leftrightarrow NO_{(ads)} + H_2O_{(l)} \quad (12)$$

$$HNO_{3\,(aq)} + 2NO_{(ads)} + H_2O_{(l)} \leftrightarrow 3HNO_{2\,(ads)} \quad (13)$$

whereas for $[HNO_3] > 8$ mol $L^{-1}$, the following reaction mechanisms was proposed:

$$HNO_{2\,(ads)} + H^{+}_{(aq)} + e^{-} \leftrightarrow NO_{(ads)} + H_2O_{(l)} \quad (12)$$

$$HNO_{3\,(aq)} + NO_{(ads)} \leftrightarrow HNO_{2\,(ads)} + NO_{2\,(ads)} \quad (14)$$

Sicsic *et al*. [17] also observed that the reduction mechanism of nitric acid 4 mol $L^{-1}$ solution at 40 °C on inert electrode (platinum or gold) depends on the applied overpotential. Additionally, for $E < 0.65$ V/SHE, they observed a third mechanism, thus limiting the potential domain on which the Schmid's mechanism takes place (similar to equation (11)).

These results show that even if the concentrated nitric acid reduction mechanism is complex, it has already been quite well understood for noble electrode materials. However, the influence of ionic species such as Fe(III) arising from the dissolution of materials made of SS still requires a deeper investigation. In this work, the coupling of electrochemical methods, Raman analysis and mass spectrometry, was used to investigate the impact of Fe(III) on the reduction processes in concentrated $HNO_3$ (4 mol $L^{-1}$ at 40 °C) at gold electrode. The gas production was measured as a function of the potential and was combined to the characteristic electrochemical response of the system. Then, the influence of the concentration of Fe(III), [Fe(III)], on the reduction reaction of concentrated $HNO_3$ was deeply investigated, and experimental results were discussed in a view of the mechanisms proposed in the literature [17, 18].

## 2. Experimental

### *2.1. Electrochemical measurements*

All experiments were performed using a classical 3-electrodes configuration in a 250 mL cell. The working and the counter electrodes were a gold rotating-disk electrode with an area of 3.14 $mm^2$ and a platinum basket, respectively. The reference electrode was a mercury/mercurous sulfate electrode ($Hg/Hg_2SO_4$ – MSE, $E$ = + 0.65 V/SHE at 25 °C). For an easiest comparison with literature data, all potentials reported in this work were converted versus the standard hydrogen electrode (SHE). All the electrochemical measurements (cyclic voltammetry - CV, chronoamperommetry, electrochemical impedance spectroscopy – EIS) were performed using a VSP workstation controlled by the software EC-Lab v.10.37 (Biologic). EIS measurements were carried out on a frequency range from 100 kHz to 10 mHz, with an amplitude of 100 mV to respect the linearity of the system. A bubbling with technical argon (99.996 %) was performed during 10 to 15 min to deaerate the solution before starting each experiment.

EIS analysis, simulation and fitting were performed using an in-lab developed software based on a Simplex algorithm.

### *2.2. Mass spectrometry*

The mass spectrometer used to perform gas analysis was an Omnistar spectrometer (Pfeiffer) with a channeltron detector. The carrier gas in the reactor was technical argon. It was flowing in the gas phase of the reactor at a rate of approximatively 16 L $h^{-1}$. The analysed mass-to-charge ratios were set at 30, 44 and 46, corresponding to NO, $N_2O$ and $NO_2$, respectively. The ionic current corresponding to the gas is obtained from the electrical response of the gas pressure of the mass spectrometer.

### *2.3. µRAMAN spectroscopy*

The Raman micro-spectroscopy (μ-Raman) was performed with a LabRam HR spectrometer (Horiba) coupled with an Olympus microscope equipped with a 50× long-range objective and using a laser beam with a wavelength of 532 nm and a power output of ~5 mW. Samples were kept in small containers topped with microscope cover glasses to protect the spectrometer from $HNO_3$ fumes and, at the same time, acting as a window for Raman acquisition. μ-Raman spectra were accumulated on a Peltier-cooled CCD camera until a satisfactory signal-to-noise ratio could be obtained (typically from 60 to 300 s).

### *2.4. Chemicals*

A Millipore system was used to produce deionized water (18.2 MΩ cm) used for the preparation of all electrolytes. Nitric acid solutions were obtained by dilution of nitric acid 68% (Sigma Aldrich). Unless otherwise indicated, all experiments were performed in 4 mol $L^{-1}$ $HNO_3$ solution, and the concentration of solutions prepared was dosed by a Mettler-Toledo DL55 titrator with 1 mol $L^{-1}$ of NaOH (reagent grade, Sigma Aldrich). The Fe(III) used was purchased from VWR Chemicals as $Fe(NO_3)_3$, $9H_2O$ in order to avoid the adjunction of additional anions in the electrolyte. 2 mol $L^{-1}$ of $H_2SO_4$ solutions were prepared by dilution of sulphuric acid 96% (Acros Organics) and ferric ions were added using $Fe_2(SO_4)_3$, purchased from VWR Chemicals.

## 3. Results and Discussion

### *3.1. Role of Fe(III) on the reduction reactions of concentrated $HNO_3$*

The role of Fe(III) on the reduction mechanisms of nitric acid is not clearly understood. Two hypotheses can be put forward: a direct reduction of Fe(III) on the material or a chemical reaction involving Fe(III) in the reduction mechanisms of nitric acid. To investigate the role of Fe(III) on the reduction mechanism in concentrated nitric acid, cyclic voltammetry were performed in three solutions ($H_2SO_4$ 2 mol $L^{-1}$ + $Fe(NO_3)_3$ $5.10^{-3}$ mol $L^{-1}$, $HNO_3$ 4 mol $L^{-1}$ and

$HNO_3$ 4 mol $L^{-1}$ + $Fe(NO_3)_3$ $5.10^{-3}$ mol $L^{-1}$) at 25°C (**Figure 1**). The starting potential for each curve is indicated by a black point and the scan direction started toward cathodic potentials (the first observed peak is thus the C2' reduction peak). The experiment performed in a 2 mol $L^{-1}$ $H_2SO_4$ solution shows the electrochemical response of the Fe(III)/Fe(II) redox couple without any further reaction. The curve shows two symmetrical peaks typically observed for a reversible system, corresponding to the oxidation of Fe(II) (peak A1) and the reduction of Fe(III) (peak C1), respectively. The value of the apparent standard potential can be graphically determined (0.62 V/SHE) which is slightly inferior to the standard potential classically given in the literature ($E^0_{Fe(III)/Fe(II)}$ = 0.771 V/SHE at 25 °C in $H_2O$) [21]. The nature of the media, $H_2SO_4$ and $H_2O$ respectively, can explain this difference.

The electrochemical response in 4 mol $L^{-1}$ nitric acid solution is similar to those obtained by others authors [5, 17, 22], with some typical characteristics of this system. First, different potentials are observed for the cathodic peaks on the backward scan (C2) and forward scan (C2'). This corresponds to the different mechanisms of indirect reduction of nitric acid as discussed in the introduction. It has been shown that these mechanisms are potential-dependant and that some of them are influenced by the hydrodynamic conditions. This also explains the asymmetric behaviour between the backward and forward signals in the cathodic domain. Moreover, a single peak (A2) is observed in the anodic domain. This corresponds to the oxidation of the residual species formed during the reduction of nitric acid. It should be mentioned that the whole surface area of all the cathodic peaks is higher than the anodic area, which is in agreement with an autocatalytic process for the reduction of nitric acid (Schmid's mechanism).

When Fe(III) is added to $HNO_3$, the electrochemical response is similar in shape to the CV curve obtained without Fe(III) (**Figure 1**). In particular, no additional peak corresponding to the reduction of Fe(III) or to the oxidation of Fe(II) can be observed. However, the peak

intensities corresponding to the reduction of nitric acid are significantly larger in presence of Fe(III) showing, from a qualitative point of view, the catalytic effect of the Fe(III) species on the reduction mechanisms of concentrated nitric acid.

### *3.2. Impact of Fe(III) addition in concentrated $HNO_3$ on chemical equilibria*

Concentrated $HNO_3$ solutions are very complex media, as shown by Sicsic *et al.* [23] who has identified 16 different nitrogen species that could be present simultaneously, as gas or soluble species. μ-Raman spectroscopy analyses were performed, and the results are presented in **Figure 2**. The spectrum obtained for concentrated nitric acid is in agreement with the literature [24-28]. The bands observed at 727, 1050 and 1442 $cm^{-1}$ can be attributed to $NO_3^-$. They are ascribed to the ν4 in plane deformation, the ν1 symmetric stretch and the ν3 asymmetric stretch, respectively. The peak observed at 1644 $cm^{-1}$ corresponds to the $H_2O$ bending [28]. The concentration is too low to observe the peak due to undissociated $HNO_3$ (≈ 950 $cm^{-1}$) [28].

The evolution of the μ-Raman spectra as a function of the [Fe(III)] show that Fe(III) contributions are observed for concentration above 0.1 mol $L^{-1}$. We can assume that this value corresponds to the detection limit of the μ-Raman spectrometer. For larger concentration, two phenomena are observed. First, Fe(III) forms some complexes with water but not with nitrogen species. The corresponding bands of $[Fe(H_2O)_6]^{3+}$ are observed at 288 $cm^{-1}$ and 506 $cm^{-1}$ [29]. We assume that $Fe(NO_3)_3$ is not observed on Raman spectra because of the weak interaction between Fe(III) and nitrates [30]. As a consequence, the vibration bands are not impacted by the presence of nitrates. Moreover, the $NO_2/NO_3^-$ ratio evolves toward the formation of $NO_2$ (1300 $cm^{-1}$) [24, 26]. As Fe(III) was added in solution as a $Fe(NO_3)_3$ salt, it was confirmed that this band attribution was not due to the addition of the counter-anions $NO_3^-$, by performing

additional experiments in ($HNO_3$ + $NaNO_3$) solutions (data not shown). These spectra were notably distinct from those of the Fe(III)-containing solutions, confirming the spectral contributions due to the presence of Fe(III).

### *3.3. Reduction reactions of concentrated $HNO_3$ under Fe(III) influence*

The influence of [Fe(III)] on the reduction reactions at 40°C of concentrated $HNO_3$ (4 mol $L^{-1}$) was studied by performing chronoamperometry for 30 min at different potentials in the cathodic domain. Typically, the current reaches the steady-state after 25 min. A RDE was used in order to control the hydrodynamic conditions at the interface using a value as low as 50 rpm in order to avoid ejecting the reaction products in the bulk solution [17]. At the end of the chronoamperometry, an electrochemical impedance measurement was performed at the same potential. Simultaneously to the electrochemical experiments, a continuous analysis of the gases produced was performed by mass spectrometry. Depending on the conditions, only $NO_2$, NO and $N_2O$ were produced.

**Figure 3** shows the steady-state current/potential curve (left axis) and the simultaneous gas analysis (right axis) obtained for a 4 mol $L^{-1}$ $HNO_3$ solution. Here, a very low current density is measured over the whole potential domain and no gas is produced regarding the detection limit of the mass spectrometer. In agreement with these results, the electrochemical impedance spectra measured (data not shown) are characteristic of a highly resistive system. All these observations show that the autocatalytic reduction of concentrated nitric acid was not activated in these conditions, which is in contradiction with some similar studies of the literature [31]. The only difference with these results is the size of the RDE (5 mm of diameter in the literature and 2 mm of diameter in the present work). Such a value of the electrode dimension is in agreement with the results of Lange [18] who showed that a diameter of 2 mm is near the critical value where diffusion switches from linear (for larger electrodes) to hemispheric (for smaller

electrodes), as discussed in the introduction [18]. In that case, the efficiency of mass transfer avoids the autocatalytic process of reduction of nitric acid to take place at the smaller electrode.

**Figure 4** shows the steady-state current/potential curve and the simultaneous gas analysis for a 4 mol $L^{-1}$ $HNO_3$ solution with $10^{-1}$ mol $L^{-1}$ of Fe(III) at 50 rpm and 40°C. Three different domains of potential can be observed. For the highest potentials (0.8 V/SHE < $E$), the current remains very low and no gas can be detected. For intermediate potentials (0.4 V/SHE < $E$ < 0.8 V/SHE), the cathodic current density increases with the decrease of the potential and a production of NO gas is detected. Then, for lower potentials ($E$ < 0.4 V/SHE), a decrease of the cathodic current density is observed and both $N_2O$ and NO gases are produced simultaneously. **Figure 5** shows the Nyquist plots at different potentials corresponding to the three zones previously discussed. For E = 0.85 V/SHE (**Figure 5.a**), a capacitive loop can be seen at high frequency, with a high resistance of 66 Ω $cm^2$ and 69 Ω $cm^2$ and a capacitance of 43 μF $cm^{-2}$ and 41 μF $cm^{-2}$ (ascribed to the double-layer capacitance [32] in parallel with a charge transfer resistance) at 50 rpm and 100 rpm, respectively. Moreover, an inductive loop is observed for lower frequencies and the different rotation rates of the electrode slightly modify the Nyquist diagram for low frequencies. Additionally, the EIS response shows a time-constant in the middle frequency domain ascribed to the diffusion of electroactive species. To go further in the description of the impedance diagrams, the mechanisms described in the introduction were considered. Since no reduction current and gas production was observed on this potential domain, the diffusion time-constant should be ascribed to the $HNO_2$ diffusion. Additionally, the low frequency inductive loop is characteristic of an adsorption phenomenon. The NO intermediate species is susceptible to adsorb at the surface (equations (8) and (12)). This is also in agreement with the effect of the rotation rate of the RDE that is observed on the electrochemical impedance spectra. Qualitatively, the diffusion part is bigger and the inductive loop is smaller when rotation rate increases, meaning that the reduction products are ejected

outside the diffusion layer. The high charge-transfer resistance observed means that the kinetic of the reaction is very low.

For E = 0.55 V/SHE (**Figure 5.b**), only one capacitive loop is observed at high frequency, with a smaller resistance of 1.4 Ω $cm^2$ and 2.6 Ω $cm^2$ and a capacitance of 26 µF $cm^{-2}$ and 34 µF $cm^{-2}$ (double-layer [32]) at 50 rpm and 100 rpm, respectively. For lower frequencies, a slope of 45° is clearly observed, which is characteristic of a diffusion behaviour. The Nyquist diagram is influenced by the rotation rate of the electrode, which indicates that the system is limited by the diffusion and the Schmid's mechanism dominates at this potential (equations (6) to (10)). Moreover, the higher the rotation rate, the higher the charge transfer resistance. This is consistent with a more efficient evacuation of reduction products from the diffusion layer.

For E = 0.45 V/SHE (**Figure 5.c**), the EIS spectrum shows 3 different time-constants. A first capacitive loop is observed in the high frequencies, which depends on the rotation rate of the RDE. This time-constant is attributed to the charge transfer reaction and is composed of the charge transfer resistance (1.4 Ω $cm^2$ at 50 rpm and 2.8 Ω $cm^2$ at 100 rpm) in parallel with a capacitance. The values of capacitance of 26 µF $cm^{-2}$ and 24 µF $cm^{-2}$ at 50 rpm and 100 rpm, respectively, are in agreement with typical values for a double layer capacitance in nitric acid [32]. For the intermediate frequencies, a linear part with a 45° slope indicates a typical diffusional limitation. A second capacitive loop at low frequencies, with a negative polarisation resistance (in agreement with the slope sign of the current / potential curve), is attributed to the relaxation of adsorbed species, in agreement with the production of $N_2O_{(g)}$. Moreover, the decrease of the current density shows that the autocatalytic reaction no longer occurs because of the reduction of $NO_{(ads)}$ into $N_2O_{(ads)}$, equation (11) [31]. In that case, the EIS response is influenced by the rotation rate of the electrode. Then, the diffusion limits the system, involving the Schmid's mechanism.

Experiments in a more concentrated solution, 1 mol $L^{-1}$ of Fe(III), were also performed. The current-potential steady-state curve obtained and the gas analysis are presented in **Figure 6**. A continuous increase of the current density (in absolute value) when the potential is moved towards cathodic value is obtained and the only gas produced is NO for potential smaller than 0.9 V/SHE. The Nyquist plots presented in **Figure 7** for high and low potentials, are similar. The double-layer capacitance obtained for 0.85 V/SHE and 0.25 V/SHE are respectively 10.1 μF $cm^{-2}$ and 9.4 μF $cm^{-2}$. The mechanism remains the same for all potential and the Schmid's mechanism dominates (equations (6) to (10)).

Thus, the combination of the results obtained with these different techniques shows that two behaviours are observed for the reduction mechanism of nitric acid, depending on the concentration of Fe(III) in solution and the potential. The influence of [Fe(III)] (0.1, 0.2 and 0.5 mol $L^{-1}$) is shown in **Figure 8**. For [Fe(III)] smaller than 0.2 mol $L^{-1}$, a change of mechanism is evidenced from the change of the slope of the polarization curve. Indeed, for the higher potentials (0.8 V/SHE < $E$), the reduction current is very low and no gas was detected. According to Vetter [7-9], the mechanism described by equation (1) to (5) is predominant in this potential range. For intermediate potentials (0.4-0.5 V/SHE < $E$ < 0.8 V/SHE) the Nyquist diagrams and the gas analysis (formation of NO) confirm that the Schmid's mechanism described by equations (6) to (10) is predominant. Then, for lower potentials ($E$ < 0.4-0.5 V/SHE), a third mechanism is observed, notably with the formation of $N_2O$ gas. These results are in agreement with Sicsic *et al.* [17], who also observed in pure nitric acid the formation of $N_2O$ bubbles. It should be noted that the use of high concentration of Fe(III) (1 mol.$L^{-1}$) added as $Fe(NO_3)_3$, corresponds to a significant increase of $NO_3^-$ concentration (from 4 to 7 mol.$L^{-1}$). Some experiments were performed by changing the nature of the anion or cation (data not shown) to determine the impact of $NO_3^-$ on the steady-state polarization curve. Interestingly, a

synergistic effect of [$NO_3^-$] and [Fe(III)] was observed, but as expected, the steady-state current is mostly controlled by the Fe(III) concentration.

The influence of [Fe(III)] on the charge transfer resistance as a function of potential is presented in **Figure 9**. Interestingly, these results show that as soon as Fe(III) is in solution, the charge transfer resistance is almost constant over the whole potential domain. Moreover, the value of charge transfer resistance is in the same order of magnitude for all concentrations of Fe(III), excepted for the largest one (1 mol $L^{-1}$) for which the charge transfer resistance is one order of magnitude lower. **Figure 10** show the variations of $R_t \times i$ as a function of the potential for different [Fe(III)]. By this way, we assume that if the value of $R_t \times i$ is independent from the potential, the mechanism remains the same [33]. Here, it is observed that for E = 0.85 V/SHE, for every concentrations, the value is lower than others. It is in agreement with the detection of the production of NO in whole range of potential. Then, for 1 mol $L^{-1}$ of Fe(III) the value of $R_t \times i$ is relatively independent of the potential which means the same mechanism occurs, most probably the Schmid's mechanism. For $5.10^{-1}$ mol $L^{-1}$, excluding the value of $R_t \times i$ for E = 0.15 V/SHE, it also seems to be independent of the potential. Then, for [Fe(III)] $\leq 2.10^{-1}$ $mol.^{-1}$, two behaviours are observed according to the potential, meaning that two different mechanisms occur which is in agreement with the detection of either NO alone or NO + $N_2O$. Taking into account these results, the following mechanism describing the role of Fe(III) on the reduction reaction of concentrated $HNO_3$ can be proposed:

$$Fe^{3+}{}_{(aq)} + e^- \leftrightarrow Fe^{2+}{}_{(aq)} \qquad (15)$$

$$Fe^{2+}{}_{(aq)} + \frac{3}{2}H^+{}_{(aq)} + \frac{1}{2}NO_3{}^-{}_{(aq)} \leftrightarrow Fe^{3+}{}_{(aq)} + \frac{1}{2}HNO_{2\,(aq)} + \frac{1}{2}H_2O_{(l)} \qquad (16)$$

$$HNO_{2\,(aq)} + H^+{}_{(aq)} + e^- \leftrightarrow NO_{(ads)} + H_2O_{(l)} \qquad (12)$$

After this step, two pathways are proposed depending on the electrode potential. Indeed, for high potentials (E > 0.15V/SHE), the reduction of $NO_{(ads)}$ in $HNO_{2(aq)}$ is more probable and can be described as:

$$NO_{(ads)} + \frac{1}{2}H^{+}{}_{(aq)} + \frac{1}{2}NO_3{}^{-}{}_{(aq)} + \frac{1}{2}H_2O_{(l)} \leftrightarrow \frac{3}{2}HNO_{2\,(aq)} \quad (10)$$

For the lower potential (E < 0.15V/SHE), Reactions *(11)* and *(17)* occur:

$$2NO_{(ads)} + 2H^{+}{}_{(aq)} + 2e^{-} \leftrightarrow N_2O_{(ads)} + H_2O \quad (11)$$

$$N_2O_{(ads)} \leftrightarrow N_2O_{(g)} \quad (17)$$

By comparing these equations to Vetter's and Schmid's equations ((1) to (10)), it seems that the homogeneous mechanism occurs in these conditions. Moreover, equation (12), corresponding to the formation of NO, appears to be the step of the reduction mechanism of $HNO_3$ that is indirectly impacted by the presence of Fe(III). This is due to the formation of $HNO_2$ (16), which is the main species involved in the autocatalytic reduction mechanism of $HNO_3$. This was also confirmed by the CV curves presented in **Figure 11** obtained in presence and in absence of $NO_2^-$ and is also in agreement with the work of Lange *et al.* [22].

This overall mechanism is illustrated in **Figure 12**. It also takes into account the formation of $NO_2$ observed by μ-Raman spectroscopy, which is independent from the reduction mechanism.

## 4. Conclusions

The influence of Fe(III) at different concentrations on the reduction mechanism of concentrated $HNO_3$ has been studied in this work by the coupling of electrochemical techniques (CV, chronoamperometry, EIS), Raman microspectroscopy and mass spectroscopy.

First, the use of Raman microspectroscopy at room temperature has shown that the addition of Fe(III) plays a significant role on the chemical equilibriums in the electrolytic solution by promoting the formation of reduced species of nitric acid such as $NO_2$. Moreover, it was also shown using cyclic voltammetry, that the Fe(III) has a catalytic effect on the reduction reaction of concentrated $HNO_3$. This is a direct experimental confirmation of a qualitative influence of Fe(III) on the reduction mechanism of concentrated $HNO_3$.

A detailed investigation of this electrochemical system at 40 °C has been also for solutions with different concentrations in Fe(III). The addition of Fe(III) in solution promotes the formation of $HNO_2$, leading to an increased production of NO. In such a case, the mechanism that dominates in our conditions is the Schmid's mechanism, with respect to Vetter's mechanism. According to the [Fe(III)] and to the applied potential, the mechanism is susceptible to change for lower potentials, leading to the formation of NO (autocatalysis) or to the end of the autocatalytic phenomena by forming $N_2O$. These results thus show a different response for the reduction mechanism of $HNO_3$ than those obtained without Fe(III), where both Vetter's and Schmid's mechanism can occur successively, depending on the applied potential.

# Figures

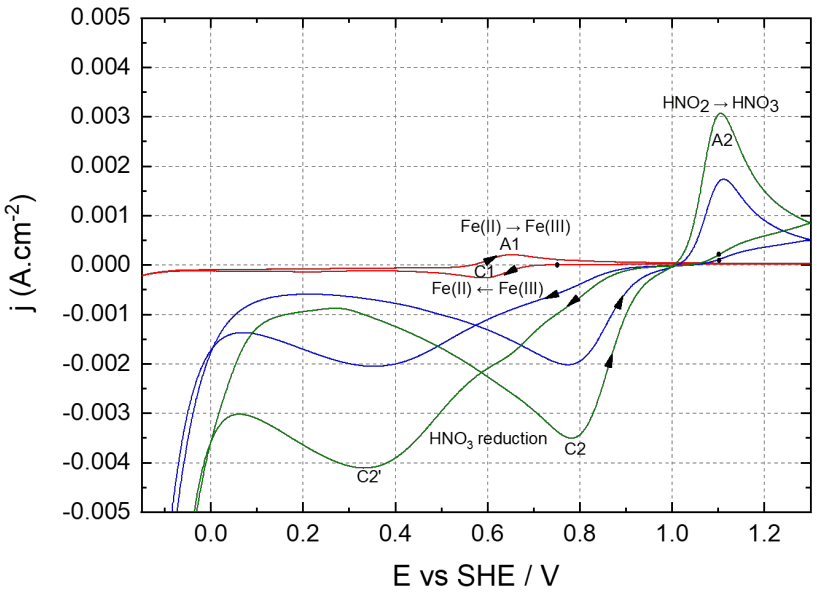


**Figure 1.** Cyclic voltammetry of $Fe_2(SO_4)_3$ $5.10^{-3}$ mol $L^{-1}$ in $H_2SO_4$ 2 mol $L^{-1}$ (red curve), $HNO_3$ 4 mol $L^{-1}$ (blue curve), and $Fe(NO_3)_3$ $5.10^{-3}$ mol $L^{-1}$ in $HNO_3$ 4 mol $L^{-1}$ (green curve). T = 25 °C, $v$ = 20 $mV.s^{-1}$. The starting potential for each curve is indicated by a black point and the scan direction started toward cathodic potentials.

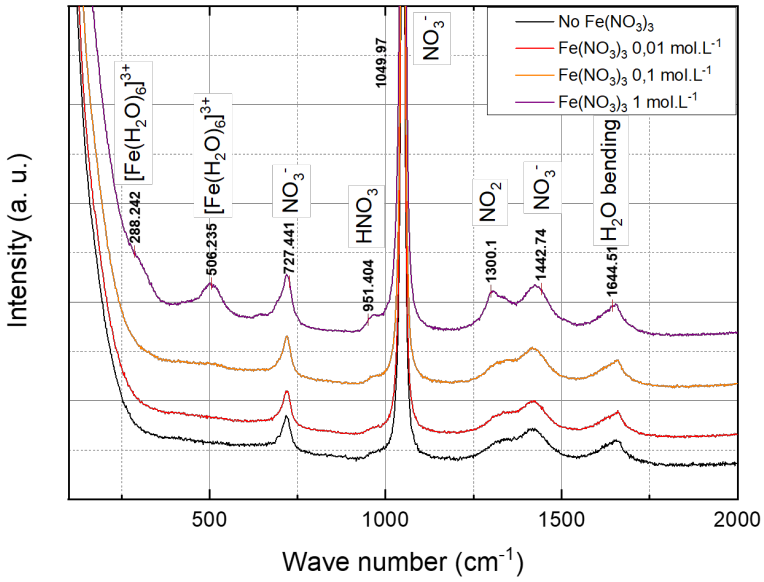


1

2 **Figure 2.** μ-RAMAN spectra of concentrated nitric acid (4 mol $L^{-1}$) with different

3 concentrations of Fe(III), at T = 25 °C.

4

5

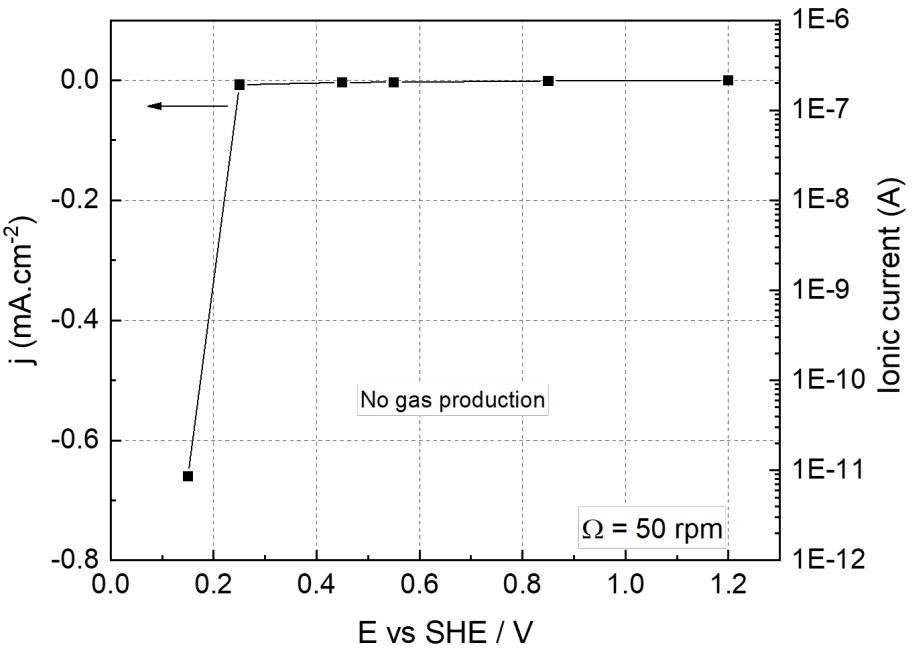


1

2 **Figure 3.** Steady-state polarisation curve for concentrated nitric acid (4 mol $L^{-1}$) without
3 $Fe(NO_3)_3$ on a gold rotating disk electrode at 50 rpm (left axis) coupled with gas analysis by
4 mass spectrometry (right axis). T = 40 °C.

5

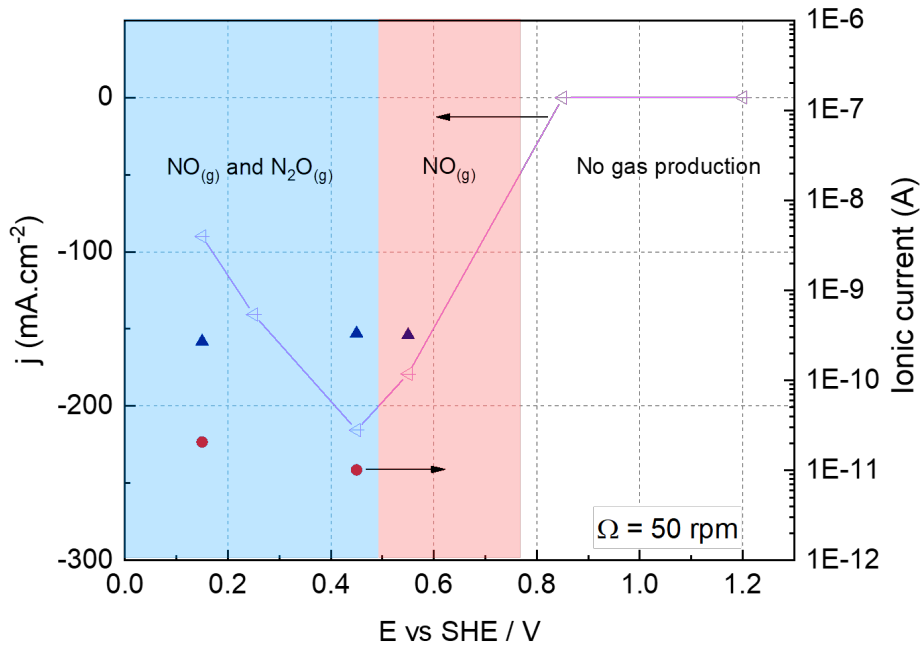


1

2 **Figure 4.** Current density of concentrated nitric acid (4 mol $L^{-1}$) with $Fe(NO_3)_3$ ($10^{-1}$ mol $L^{-1}$)
3 on gold rotating disk electrode at 50 rpm (curve - left axis) coupled with gas analysis by mass
4 spectrometry (circles and triangles - right axis). T = 40 °C.

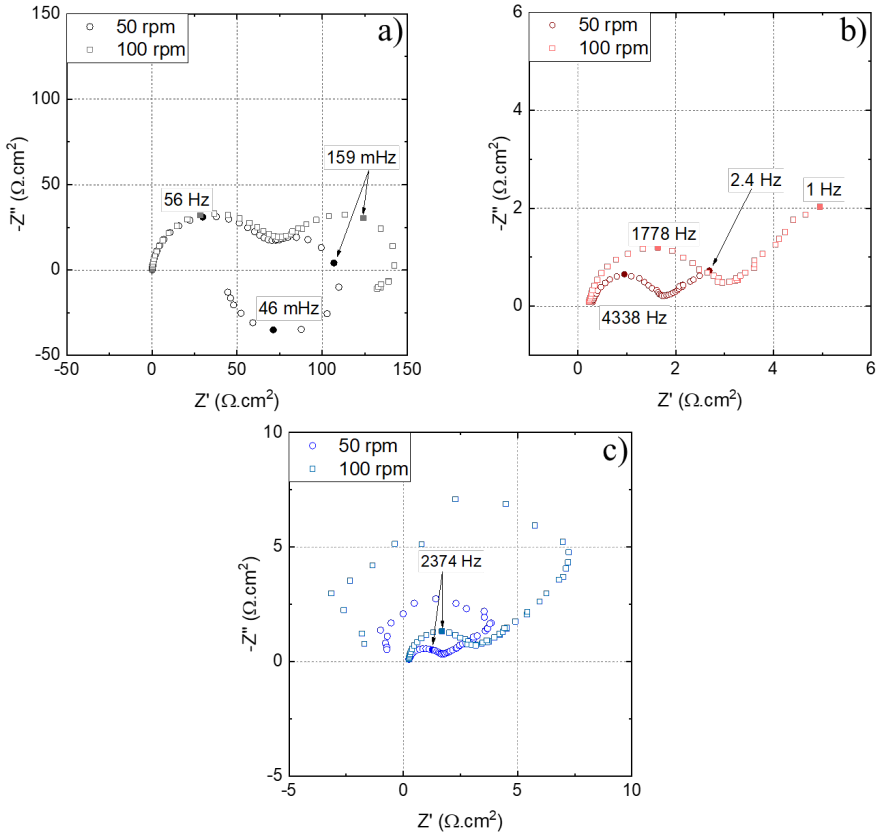


**Figure 5.** Nyquist plots obtained on gold rotating disk (50 rpm) in 4 mol $L^{-1}$ $HNO_3$ + $10^{-1}$ mol $L^{-1}$ $Fe(NO_3)_3$ solution at 0.85 V/SHE (a), 0.55 V/SHE (b) and 0.45 V/SHE (c). T = 40 °C.

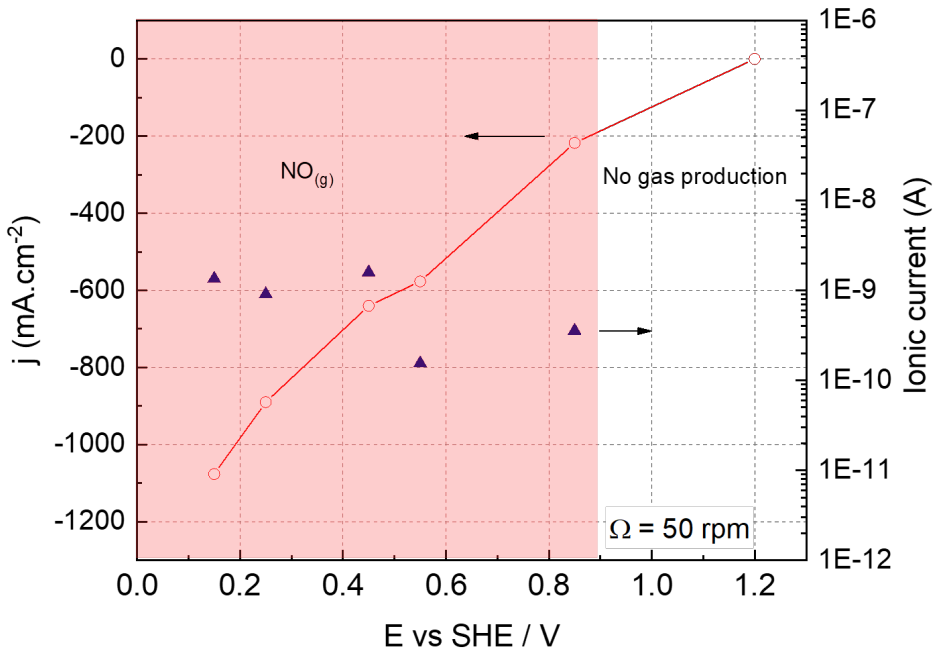


1

2 **Figure 6.** Steady-state polarization curve of concentrated nitric acid (4 mol $L^{-1}$) with $Fe(NO_3)_3$

3 (1 mol $L^{-1}$) on gold rotating disk electrode at 50 rpm (left axis) coupled with gas analysis by

4 mass spectrometry (right axis). T = 40 °C.

5

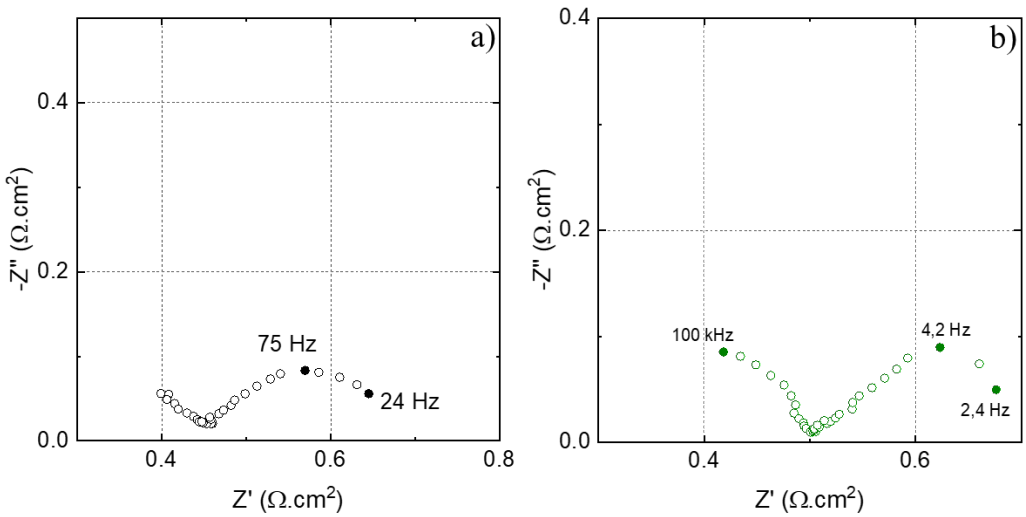


1

2 **Figure 7.** Nyquist plot obtained on gold rotating disk (50 rpm) in 4 mol $L^{-1}$ $HNO_3$ + 1 mol $L^{-1}$

3 $Fe(NO_3)_3$ solution at 0.85 V/SHE (a) and 0.25 V/SHE (b).

4

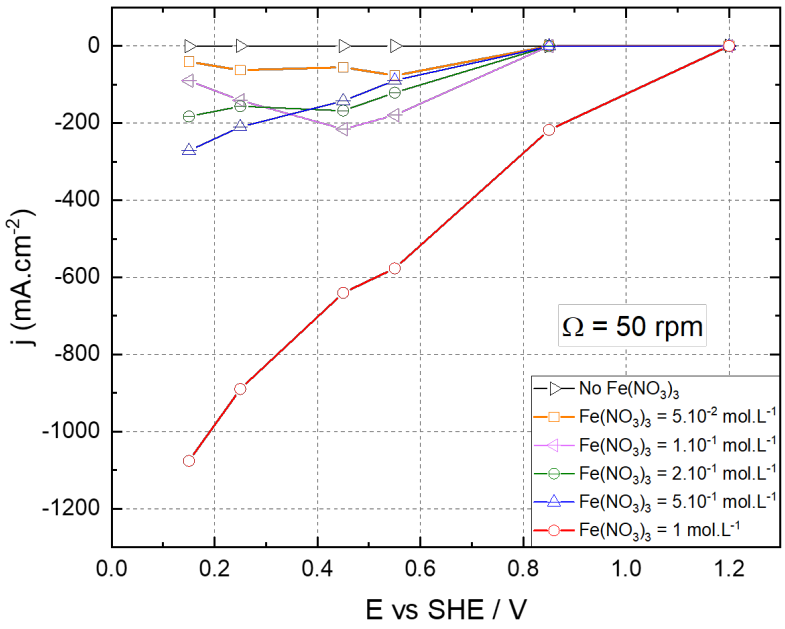


5

6 **Figure 8.** Steady-state polarisation curves of concentrated nitric acid (4 mol $L^{-1}$) with

7 different concentration of $Fe(NO_3)_3$ on gold rotating-disk at 50 rpm. T = 40 °C.

8

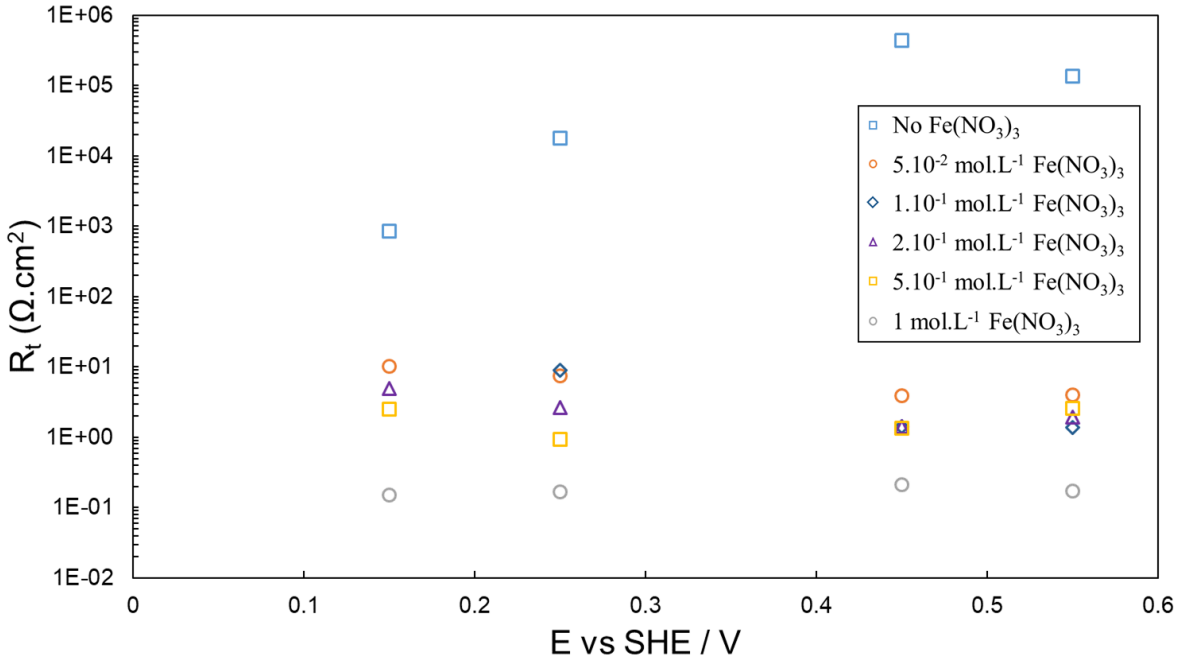


**Figure 9.** Evolution of $R_t$ as a function of the potential for concentrated nitric acid (4 mol $L^{-1}$) with different concentrations of $Fe(NO_3)_3$. 50 rpm, T = 40 °C.

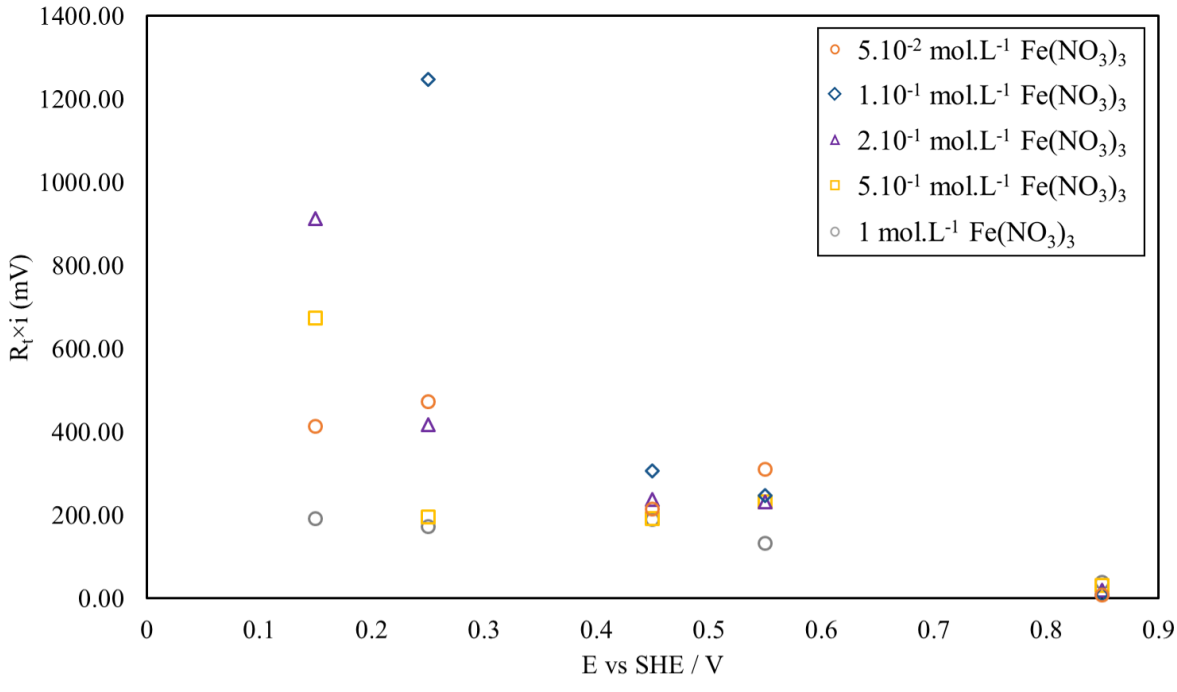


**Figure 10.** Evolution of $R_t$×i as a function of the potential in concentrated nitric acid (4 mol $L^{-1}$) with different concentrations of $Fe(NO_3)_3$. 50 rpm, T = 40 °C.

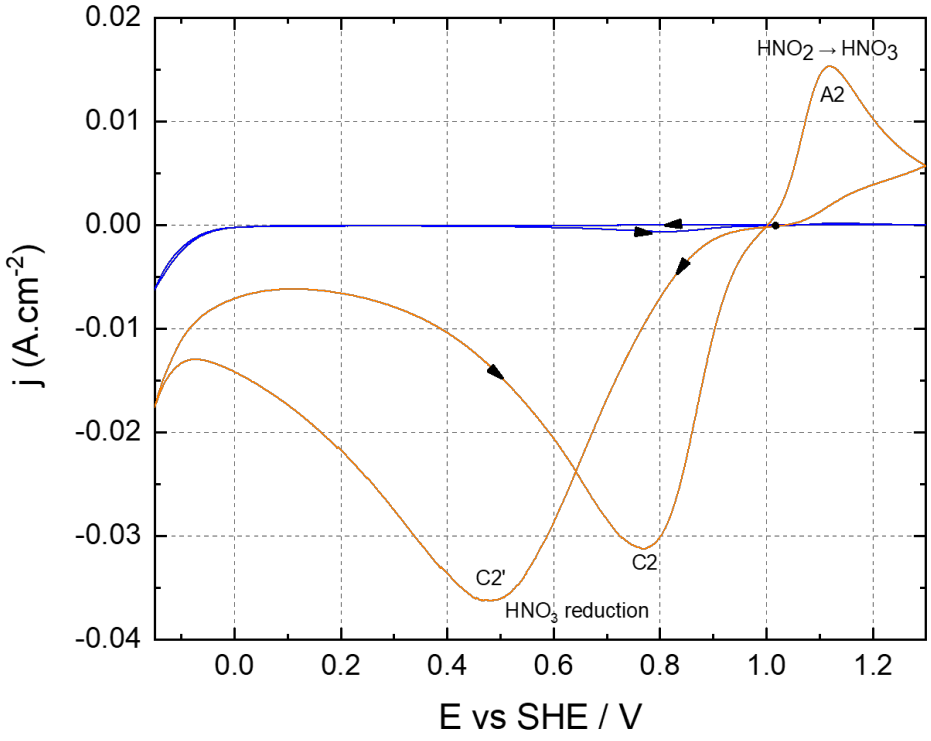


**Figure 11.** CV curves of 4 mol.L$^{-1}$ $HNO_3$ (blue curve) and 4 mol.L$^{-1}$ $HNO_3$ + $10^{-2}$ mol.L$^{-1}$ $NaNO_2$ (orange curve) at T = 40 °C and $v$ = 20 mV/s$^{-1}$. The starting potential for each curve is indicated by a black point and the scan direction started toward cathodic potentials.

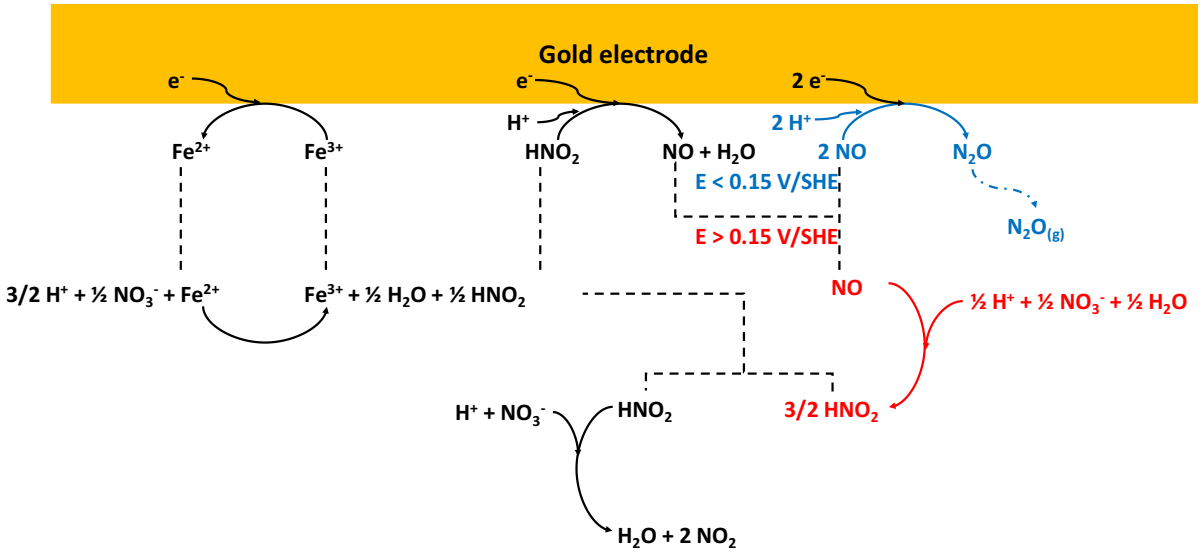


**Figure 12.** General scheme for the reduction mechanism of concentrated $HNO_3$ (4 mol L$^{-1}$) in presence of Fe(III) at 40 °C.

1

1. Jayaraj, J., et al., *Microstructure and Corrosion Behavior of Hf-40 Wt Pct Ti Alloy in Nitric Acid Medium for Reprocessing Applications.* Metallurgical and Materials Transactions A: Physical Metallurgy and Materials Science, 2016. **47**(9): p. 4393-4403.
2. Fauvet, P., *Corrosion issues in nuclear fuel reprocessing plants*, in *Nuclear corrosion science and engineering*, D. Feron, Editor. 2012, Woodhead Publishing. p. 679-728.
3. Gwinner, B., et al., *Towards a reliable determination of the intergranular corrosion rate of austenitic stainless steel in oxidizing media.* Corrosion Science, 2016. **107**: p. 60-75.
4. Gwinner, B., et al., *A stereological approach for measuring the groove angles of intergranular corrosion.* Corrosion Science, 2017. **115**: p. 1-7.
5. Balbaud, F., et al., *Mechanism of corrosion of AISI 304L stainless steel in the presence of nitric acid condensates.* Corrosion Science, 2000. **42**(10): p. 1685-1707.
6. Fauvet, P., *19 - Corrosion issues in nuclear fuel reprocessing plants*, in *Nuclear Corrosion Science and Engineering*, D. Féron, Editor. 2012, Woodhead Publishing. p. 679-728.
7. Vetter, K., *Uber den enstellungsmechanismus des HNO2/HNO3 redoxpotentials.* Z.Phys.Chem., 1950. **194**: p. 199-206.
8. Vetter, K., *Die Abhängigkeit der Anfangsneigung der Stromdichte-Potentialkurve von den Konzentrationen,Rückschlüsse auf den potentilbestimmenden Vorgang bei Redoxsystemen.* Z.Phys.Chem., 1950. **194**: p. 284-296.
9. Vetter, K.J., *Entgegnung auf die vorstehende Arbeit von G.Schmid über « Die autokatalytische Natur der kathodischen Reduktion von Salpetersäure zu salpetriger Säure ».* Zeitschrift für Elektrochemie, 1959. **63**(9): p. 1189-1191.
10. Schmid, G., *Die autokatalytische Natur de kathodischen Reduktion von Salpetersäure zu salpetriger Säure. I.Zur Deutung stationärer Strom-Spannungs-Kurven.* Zeitschrift für Elektrochemie, 1959. **63**(9): p. 1183-1188.
11. Schmid, G. and J. Delfs, *Die autokatalytische Natur der kathodischen Reduktion von Salpetersäure zu salpetriger Säure. II.Der galvanostatische Einschaltvorgang.* Zeitschrift für Elektrochemie, 1959. **63**(9).
12. Schmid, G., *Die autokatalytische Natur der kathodischen Reduktion von Salpetersäure zu salpetriger Säure. III.Mathematische Behandlung einer autokatalytischen Elektrodenreaktion 1.Ordnung.* Zeitschrift für Elektrochemie, 1961. **65**(6): p. 531-534.
13. Schmid, G., *Die autokatalytische Natur der kathodischen Reduktion von Salpetersäure zu salpetri¬ger Säure. IV. Der potentiostatische Einschaltvorgang.* Ber. Bunsengesellschaft physik Chem, 1964. **68**(7): p. 677-688.
14. Schmid, G., *Das Verhalten von salpetriger und Salpetersäure an der rotierenden Scheibenelektrode. I. HNO2 in schwefelsauren Lösungen ohne HNO3-Zusatz.* Berichte der Bunsengesellschaft, 1969. **73**(2): p. 189-199.
15. Razygraev, V.P., *Certain characteristics of the cathodic reduction of nitric acid on a platinum electrode.* Doklady Akademii nauk SSSR, 1986. **288**(6): p. 1428-1432.
16. Pourbaix, M., *Atlas of Electrochemical Equilibria in Aqueous Solutions*. 1966: National Association of Corrosion Engineers.
17. Sicsic, D., F. Balbaud-Celerier, and B. Tribollet, *Mechanism of Nitric Acid Reduction and Kinetic Modelling.* European Journal of Inorganic Chemistry, 2014(36): p. 6174-6184.
18. Lange, R., *Phénomènes de couplage acier 304L – platinoïdes dans les milieux de dissolution des combustibles usés. Ph.D*. 2012, Université Pierre et Marie Curie. p. 174.

19. Brett, C.M.A. and A.M.O. Brett, *Electrochemistry: Principles, Methods, and Applications*. 1993: Oxford University Press. 444.
20. Balbaud, F., et al., *Cathodic reactions involved in corrosion processes occurring in concentrated nitric acid at 100 degrees C.* European Journal of Inorganic Chemistry, 2000(4): p. 665-674.
21. Pourbaix, M., *Atlas d'équilibres électrochimiques. Section 18.1 : Azote*, ed. v. Gauthier. 1963.
22. Lange, R., et al., *On the kinetics of the nitrate reduction in concentrated nitric acid.* Electrochemistry Communications, 2013. **29**(0): p. 25-28.
23. Sicsic, D., F. Balbaud-Célérier, and B. Tribollet, *Modelling of the nitric acid reduction process: application to materials behavior in reprocessing plants*, in *ICAPP '12*. 2012: Chicago, USA.
24. Kato, C., K. Kiuchi, and K. Sugimoto, *Thermodynamic study on redox reactions of boiling nitric acid solutions.* Corrosion Engineering, 2003. **52**(1): p. 69-85.
25. Ruas, A., et al., *Nitric acid: modeling osmotic coefficients and acid-base dissociation using the BIMSA theory.* Dalton Transactions, 2010. **39**(42): p. 10148-10153.
26. Stern, S.A., J.T. Mullhaupt, and W.B. Kay, *The Physicochemical Properties of Pure Nitric Acid.* Chemical Reviews, 1960. **60**(2): p. 185.
27. A. Zhang, J.H., X. Zhang, F. Wang, *Hydroxylamine derivatives in Purex Process: I. Study on the kinetics of redox reaction between N,N-diethylhydroxylamine and nitrous acid.* Journal of Radioanalytical and Nuclear Chemistry, 1998. **230**: p. 5.
28. G. L. Nelson, A.M.L., A. J. Casella, J. M. Bello, S. A. Bryan, *Development and testing of a novel micro-Raman probe and application of calibration method for the quantitative analysis of microfluidic nitric acid streams.* Royal Society of Chemistry, 2018. **143**: p. 1188-1196.
29. An, K.-y., Y.-x. Wang, and X.-w. Zhang, *A study on stainless steel causticity by mobile electrochemical corrosion.* Wuran Fangzhi Jishu, 2014. **27**(6): p. 20-24.
30. Bond, W.D., Y. Jao, and R. Peterson, *The oxidation-reduction kinetics involved in the Np(V)+Fe(II)=Np(IV)+Fe(III) system in nitric acid solutions.* Journal inorganic nuclear chem., 1977. **39**: p. 1395-1402.
31. Sicsic, D., *Modélisation thermodynamique et cinétique de la réduction de l'acide nitrique concentré*, in *DEN/DANS/DPC/SCCME/LECNA*. 2011, Université Pierre et Marie Curie. p. 148.
32. Su, H., et al., *Machine learning models for solvent effects on electric double layer capacitance.* Chemical Engineering Science, 2019. **202**: p. 186-193.
33. Caprani, A. and J.P. Frayret, *Behaviour of titanium in concentrated hydrochloric acid: dissolution-passivation mechanism.* Electrochimica Acta, 1979. **24**(8): p. 835-842.